Accepted manuscript (author version)

To appear in:

Iranian Journal of Earth Sciences (Iran J. Earth. Sci.)

E-ISSN: 2228-785X Print ISSN: 2008-8779

Received: 25 September 2024

Revised: 30 April 2025

Accepted: 14 September 2025

DOI: https://doi.org/10.57647/j.ijes.2025.17568

Original Research

Evolution of ore-forming fluids at the Hesar gold deposit, NW Iran: Constraints from fluid inclusions and stable isotopes (O,S)

Mohammad Yousefi[1], Nima Nezafati[2], Nematollah Rashidnejad-Omran[3*], Mohammad Lotfi[4], Peyman Afzal[5], Majid Ghaderi[6]

[1] Department of Earth Sciences, Science and Research Branch, Islamic Azad University, Tehran, Iran
[2] Deutsches Bergbau-Museum, Bochum, Germany
[3] Department of Petrology, Tarbiat Modares University, Tehran, Iran
[4] Geological Survey of Iran, Tehran, Iran
[5] Department of Petroleum and Mining Engineering, South Tehran Branch, Islamic Azad University, Tehran, Iran
[6] Department of Economic Geology, Tarbiat Modares University, Tehran, Iran

* Corresponding author: rashid@modares.ac.ir

Abstract

The Hesar gold mining area is located in the Alborz-Azerbaijan zone. The dominant lithology in the Hesar mineral range includes andesite-trachyandesite, basalt, dacitic tuff, and rhyodacite in the form of stocks and dikes. Mineralization in the Hesar gold mineral range has occurred between marbles formed by the metamorphism of limestone and dolomite. Ore formation in the Hesar gold mineral range has taken place in fractures, cracks, and voids of the Eocene-aged host rock. The gold mineralization is associated with pyrite, arsenopyrite, iron hydroxide, and quartz gangue minerals, forming a mineral paragenesis. The dominant textures and structures in this deposit include cavity-filling, veinlet, replacement, and disseminated textures. Based on petrographic studies of fluid inclusions in quartz minerals, five types of fluid inclusions were identified based on their phase type and number, including: 1. Type 1: Single-phase liquid (L), 2. Type 2: Single-phase vapor (V), 3. Type 3: Two-phase liquid-rich (L+V), 4. Type 4: Two-phase vapor-rich (V+L), 5. Type 5: Three-phase with a solid phase (L+V+S). Microthermometric studies of the fluid inclusions revealed a homogenization temperature ranging from 66 to 266°C, and a salinity of 0.8 to 14 wt.% NaCl equivalent. Additionally, the mineralization process occurred at a depth of less than 600 meters below the Earth's surface and under a pressure of less than 10 bar. Moreover, Raman spectroscopy on several fluid inclusion samples demonstrated correlating results with those of microthermometric measurements. The $\delta^{34}S$ values in pyrite, ranging from 7.6‰ to -2.8‰, indicate a magmatic origin for sulfur. This confirms that the pyrite, arsenopyrite, and gold

mineralization in this mineral district are genetically linked to magmatic processes. The fluid in equilibrium with quartz at 144°C exhibits $\delta_{18}O$ values between +1.9‰ and +5.2‰. This $\delta_{18}O$ range places the fluid predominantly within the compositional fields of meteoric waters and subvolcanic granitic rocks, suggesting significant contribution from these sources. Based on data obtained from the Hesar study area, the mineralizing fluid is of magmatic origin, formed through mixing with meteoric waters. The genesis of the Hesar gold mineralization likely belongs to the category of epithermal deposits.

Keywords: Fluid inclusions, Raman spectroscopy, Hesar, Epithermal, Isotopes

1. Introduction

The Hesar gold-copper prospecting area is located southwest of Mianeh, within the Alborz-Azerbaijan structural zones of northwestern Iran. The Alborz-Azerbaijan belt is known to have a high potential for metallic ores, especially epithermal-porphyry Au-Cu (Richards 2015; Richards and Sholeh 2016). Some of the known epithermal Au deposits in Iran are epithermal deposits of the Arasbaran region (Masjed Daghi, Sharafabad, Zaglic, Safikhanlou; (Alirezaei et al. 2008; 2011), Sari Gunay (Richards et al. 2015), Gandi and Abolhassani (Shamanian et al. 2004), Arghash (Ashrafpour et al. 2012), Chah Zard (Kouhestani et al. 2015), Chahnaly (Sholeh et al. 2016), Zarshuran (Asadi et al. 2000), Glojeh (Mehrabi et al. 2016; Fig. 1b).

The study of hydrothermal fluids thermodynamic and physicochemical conditions and play a significant role in the formation of metallic deposits (Hitzman 2000). These fluids transport and precipitate this precious metal at economic concentrations in different ores (Hedenquist and Lowenstern 1994; Barnes 1997; Simon and Ripley 2011; Mishra et al. 2018; Bark et al. 2020; Jiang et al. 2020). However, However, natural data of gold contents in fluids are very occasional due to difficulties of direct access to geothermal fluid sample's deep, rarity of representative fluid inclusions trapped in minerals, and analytical limitations for this chemically composition. In addition, it is difficult to quantify the capacity of the fluids to transport gold and the factors controlling the sources, formation, and distribution of economic resources for gold and associated metals (Pokrovski et al. 2014; Liu et al. 2019).

Compositional analysis of brines within minerals deposited from hydrothermal fluids is an effective technique for obtaining physicochemical properties of the mineralizing fluids (Giles and Marshall 2004, Jebeli et al. 2020). The study of fluid inclusions as residues of paleo-brines provides comprehensive information on density, pressure, temperature, depth, salinity, and type of mineralization, as well as the volume of solutes in the fluid (Roedder 1984; Shepherd et al. 1985). Given the lack of comprehensive genetic studies, the absence of suitable drill cores for deep investigation, and the presence of evidence supporting the area's mineralization potential, the authors deemed it necessary to undertake research in this area.

This study aims to characterize the ore fluids that gave rise to the Hesar gold deposit using Raman spectroscopy data in combination with fluid inclusions and stable isotopes to understand the formation conditions of the deposit, including the physical conditions, and the sources of the fluids and type of mineralization

2. Geological Setting

2.1. Regional Geology

Subduction of the Neo-Tethyan Oceanic lithosphere beneath the Iranian plate has resulted in the formation of a different tectono-magmatic zones, including Urumieh-Dokhtar Magmatic Arc (UDMA) and Alborz-Azerbaijan Magmatic Belt (AMB) and related ore systems. Arasbaran, and East Iran Magmatic Assemblage (EIMA), as illustrated in Fig. 1. These magmatic activities, located in the middle part of the Alpine-Himalayan orogenic belt, occurred through the NE direction subduction of the Neo-Tethyan Ocean beneath the Iranian plate (Stöcklin 1974; Berberian and King 1981; Stampfli 2000). According to Aghazadeh et al. (2015) and Richards and Sholeh (2016), porphyry Cu (Mo-Au) deposits in Iran were developed during the upper Eocene (39–37 Ma), and upper Oligocene (29–27 Ma) to Miocene (18–6 Ma). These deposits mainly formed in the Arasbaran, EIMA, and UDMA (Zarasvandi et al. 2005; Shafiei et al. 2009; Haschke et al. 2010; Aghazadeh et al. 2015; Hassanpour and Moazzen 2017; Aliyari et al. 2020; Shahbazi et al. 2021).

The AMB is a magmatic belt that occurred through the subduction of the Neo-Tethyan Ocean during the convergence of the Eurasian and Arabian plates (Stöcklin 1974; Asiabanha and Foden 2012; Nabatian et al. 2014; Ashrafi et al. 2018) (Fig. 1). There are many Au, Cu, Pb-Zn, and Fe deposits in this magmatic belt. However, except for the Chodarchay Au-Cu deposit (Yasami et al. 2017; Yasami and Ghaderi 2019; Mousavi Motlagh et al. 2021), there are no other reports of porphyry mineralization in the AMB magmatic belt related to the evolution of the Tethyan Ocean (Aghanabati, 2004).

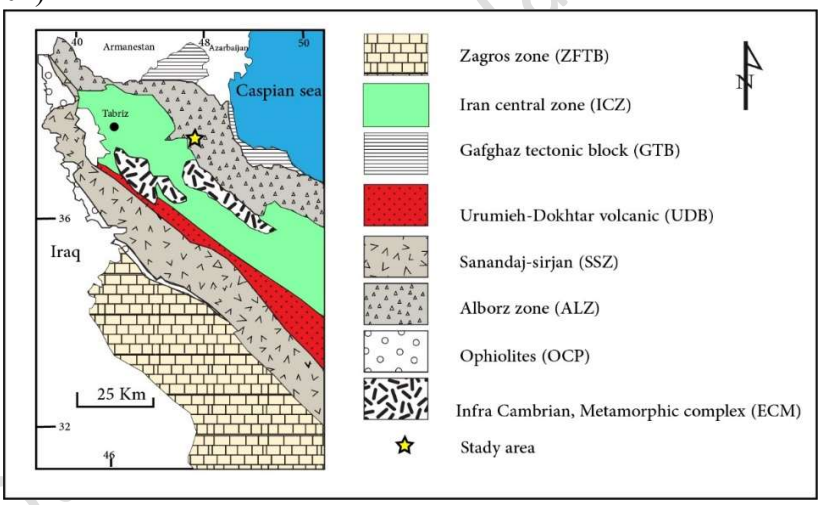

Fig. 1. Simplified structural map of Iran (Aghanabati, 2004).

Eocene volcanics include a collection of pyroclastic rocks and marine lavas, most of which are of the Middle Eocene age called the Karaj Formation based on Iranian stratigraphy (Stöcklin and Eftekhar Nezhad 1969).

Almost all outcrops in the region are composed of Cenozoic volcanic and sedimentary rocks that formed following the Laramide orogenic phase. As a result, this expansion phase of volcanic lava erupted from several fissures. These volcanic rocks include latite, trachy-andesite, andesite, basalt, dacite, and rhyolite along with pyroclastic rocks, and are part of the alkaline/shoshonitic series.

Based on the available information, the Eocene volcanics of Alborz, Armenia, and Azerbaijan are comparable, and the absence of typical calc-alkaline lavas is the hallmark of the Azerbaijan-Alborz

Volcanic Belt of the small Caucasus, which can be divided into two types including sodic and potassic types (Aghazadeh et al. 2015). However, the outcrops in this region can structurally be divided into two parts, north, and south, as a function of faults. From a structural point of view, this region is a part of the Alborz-Azerbaijan volcanic belt, which is associated with the intense activity of Tertiary volcanism. The trend of these strata is NE-SW and all the lava layers and subvolcanic domes have the same axis direction. The volcanic rocks of the western part have been infiltrated by different lava flows and dacite lavas in different forms of domes and in some places, are covered by Pliocene sediments (Hassanpour and Moazzen 2017). These units could be the main source of possible gold in the region. These deposits are folded by the Late Alpine phases, forming regular anticlines and synclines in an NW-SE direction. This basin is unconformably covered on all sides by less folded Pliocene sediments. The existence of these deformations can be attributed to the Late Miocene Alpine orogenic movements. Fault function causes uplift, displacement, removal, recurrence, and sometimes the emergence of younger dacite-rhyolite lavas which alter older lavas (Nabatian et al. 2014; Shahbazi et al. 2019; 2021).

Epithermal metallic ore deposits such as gold and copper occurred during the tectonic transition towards extensional back-arc regimes within a variation of volcanoclastic host rocks in this region (Ghasemi Siani et al. 2020). Based on previous studies, E-W, NW-SE, and NE-SW faults are the ore-controlling structures, particularly for gold mineralization (Rabiee et al. 2019; Shahbazi et al. 2019; Ghasemi Siani et al. 2020). There are many epithermal gold deposits of high-, intermediate- and low-sulfidation types such as Zehabad (Shahbazi et al. 2019; 2021), Abbasabad (Kouhestani et al. 2020), Chargar (Mousavi Motlagh and Ghaderi 2019), and Chodarchay (Yasami et al. 2017) in the region.

2.2. Local Geology

The Eocene volcanic rock complex is the oldest known unit in the Hesar mineral area. This unit is mainly composed of purple porphyry rocks with some tuff. These rocks contain plagioclase minerals in hand samples and are often altered. In microscopic studies of these rocks, trachyandesite, andesite are named and sometimes analcime feldspathoid is also seen in them. The thickness of this unit reaches several hundred meters in the center and north of the area, which is conformably overlying the underlying unit.

Oligocene to Miocene white rhyolite to rhyodacite domes and flows that cut older lavas. These rocks often have a porphyry texture and sometimes occur as ignimbrite flows. The main minerals are alkaline quartz feldspar, plagioclase, and biotite in a glassy to microcrystalline groundmass. In most places, layers of white acidic tuffs are seen below this unit. Stocks of it can be seen in the center and north of the range among the Eocene unit. This unit can be a source of hydrothermal solutions for the production of metal mineralization and silicic-sericite alterations in the area and metal mineralization. Volcanic rocks are composed of latite to trachyandesite and have a megaporphyry texture. This rock unit hosts copper and gold mineralization in the area (Fig. 2).

Also, in some parts, conglomerate units, sand, clay and limestone layers are seen along with tuff and pyroclastic rocks of Pliocene age. On these units, in some places, sediments and deposits of the present age are placed discontinuously.

Gold mineralization in the study area is not visible to the naked eye. However, field investigations revealed the presence of pyrite and chalcopyrite within quartz veins and veinlets hosted in volcanic

units and stocks. This association reinforced indications of gold mineralization, which was subsequently confirmed through sampling and laboratory studies.

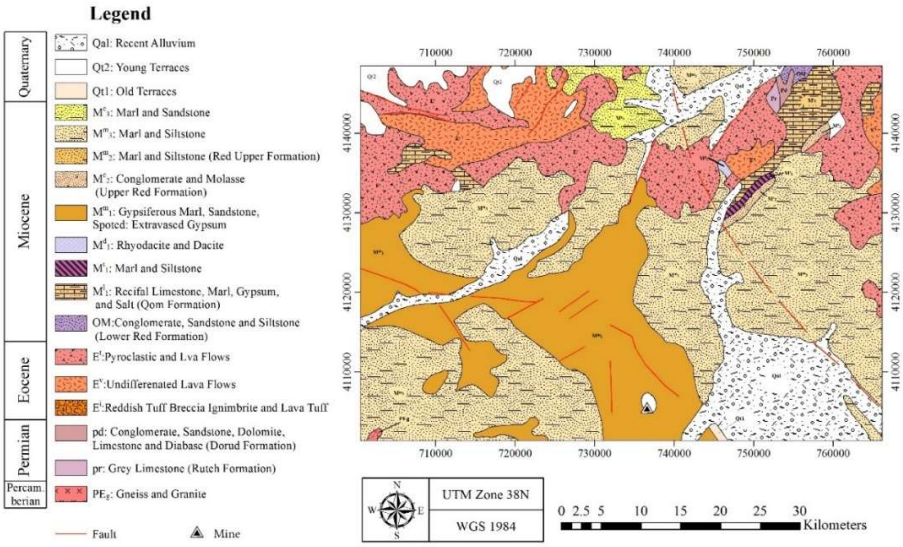

Fig.2 Geological map of a wider region of the study area taken from the 1: 250,000 Mianeh (modified Alavy et al., 1979)

3. Materials and Methods

Thirty samples of least altered, mineralized, and altered rocks were collected during field investigations from the Hesar area. For petrographic characterization and alteration mapping, fifteen thin sections of host rocks were prepared. Additionally, fifteen polished thin sections were made to analyze spatial/textural relationships between mineralization and (a) proximal wallrock, and (b) primary source lithologies. Suitable sections were selected for detailed study using Zeiss 1450vp SEM, in the partow rayan rastak The SEM-FEI Quanta 200 studies were conducted using beamcurrents between 3 and 10 nm, and electron acceleration potentials of 3–30 kV.

Furthermore, 20 samples from intersected quartz veins including gold-bearing ores were selected and double-polished sections were prepared. Microthermometry was performed on 108 primary fluid inclusions from the study area by Linkam THMSG 600 device in the fluid inclusion laboratory at Tarbiat Modares University, Tehran, Iran. This instrument can measure temperatures in the range of -196 to +600°C.

Microthermometric studies including freezing and heating were carried out on the fluid inclusion samples from the Hesar prospecting area. The final freezing of the fluid inclusions was performed in the temperature range between -100 and -105°C. The temperature is then raised until the detection of the first melting point ice ($T_m f$), which indicates the solutes in the sample. As the temperature continues to rise, the ice in the fluid inclusion melts until the last ice crystal melts which is called the final melting point ($T_m ice$). The $T_m ice$ indicates the amount of salinity (weight percentage of the NaCl equivalent). Then, the heating operation is commenced and continued as this temperature increases until the homogenization of the vapor bubbles, which is called homogenization temperature (T_h). The T_h indicates the minimum temperature of mineralization.

Calibrations were made using cesium nitrate (melting point of +414°C), n-Hexane (freezing point of −94.3°C), and synthetic fluid inclusion standards. The heating rate was 5–10°C/min at higher temperatures (>100°C), with a reproducibility of ±1°C, but was reduced to 0.1–0.5°C/min near phase transformation, with a reproducibility of ±0.1°C. Salinities of liquid-rich fluid inclusions were calculated using the measured last ice-melting temperatures.

Raman spectroscopy is a technique for solid, liquid, and gas molecular research. The molecules are visible by laser light and show three distinctive behaviors including Rayleigh, Stokes, and anti-Stokes (Van den Kerkhof 1988; McMillan 1989; Long 2002). Raman operation utilizes two effects consisting of Stokes and anti-Stokes. Raman point analysis was also carried out to obtain the exact gaseous composition of the fluid inclusions. According to the petrographic studies of the fluid inclusions, four samples were analyzed at the Leoben University in Austria to determine the fluid and gas composition of the fluid inclusions. Due to the small size of the inclusions only eight points were measured. All analyzes were performed by the Jobin Yvon LABRAM confocal-Raman spectrometer laser spectroscopy machine at the University of Leuven's Fluid Inclusion Laboratory, Austria. This device is equipped with an Nd-032/42 YAG nanometer laser. The Jobin Yvon LABRAM confocal-Raman spectrometer equipped with a frequency-doubled Nd-YAG laser (100 mW, 514 nm).

Increasing salinity has a direct relationship with decreasing I_{3260} causing an increase in I_{3425}. The I_{3260} and I_{3425} were estimated based on diagrams for H_2O samples of Raman shifts for three samples of type C fluid inclusions. The I_{3425}/I_{3260} ratio was then determined for these three samples and their molality was calculated using the standard diagram.

In this study, six pyrite and four Chalcopyrite samples from quartz veins were sulfur isotope analyzed at the Arak University for their sulfur isotope composition and thirteen quartz samples for their oxygen isotope signature.

After combustion of the bulk sample in the elemental analyzer, the generated SO_2 gas passes through the system and column and is stripped of the water in the water trap as well as SO_2 in the purge and trap column. The adsorption column is then heated to 220℃ to release any accumulated SO_2 gas. This gas ultimately enters the IRMS. In EA-IRMS, the mass ratio of 66/64 is determined to evaluate the $^{34}S/^{32}S$ ratio of the sample.

To verify the whole procedure and calibrate the reference gasses, repetitive measurements have been made on secondary laboratory standards traceable to IAEA reference material. The accepted $\delta^{34}S$ value for this standard is -6.25 ± 0.16 vs. VCDT. The instrumental accepted value for $\delta^{34}S$ standard deviation (1σ) is 0.2‰.

For $\delta^{18}O$ analysis, eight mineralized quartz samples – previously characterized for temperature and salinity – were equilibrated with CO_2 gas. The resulting CO_2 was introduced via dual-inlet isotope ratio mass spectrometry (IRMS), where $^{18}O/^{16}O$ ratios were determined by measuring m/z 46/44 ion beam intensities.

The samples under study were first crushed by a jaw crusher to remove the necessary amounts for powdering. In the next step, an attempt was made to separate the samples with less contamination from the crushed samples using a binocular microscope. After separation, the samples were powdered in an agate mortar and about one gram of them was selected for analysis.

4. Results

4.1. Mineralization stages, alteration and paragenesis

The initial prospecting throughout the area shows that mineralization and siliceous alteration types have mostly occurred between trachy-andesite, basaltic andesite, and rhyolite subvolcanic rocks (Fig. 3). The ore minerals include pyrite, arsenopyrite, and magnetite, as well as iron oxides and hydroxides, as shown in Fig. 4.

There are two phases of mineralization including oxidic and sulfidic. A siliceous zone contains gold ores in the Hesar system. Free particles of gold exist in the silicic veins and veinlets. Iron oxides specifically magnetite occurred in the first phase. Martite is also formed by the oxidation of magnetite, as shown in Fig. 5a- b. The second phase consists of sulfide ore minerals, especially pyrite and arsenopyrite. Oxide minerals, such as goethite, exist in this phase due to the oxidation of sulfide minerals. Pyrite and arsenopyrite have been oxidized and deformed to iron oxides and hydroxides, particularly goethite.

A gold particle is shown in a silicic vein in the samples by microscope and Scanning Electron Microscope (SEM; Fig. 4d).

Fig. 3. (a) rhyolite dome, (b) alteration bed rock with mineralization zon (c) vein with mineralization

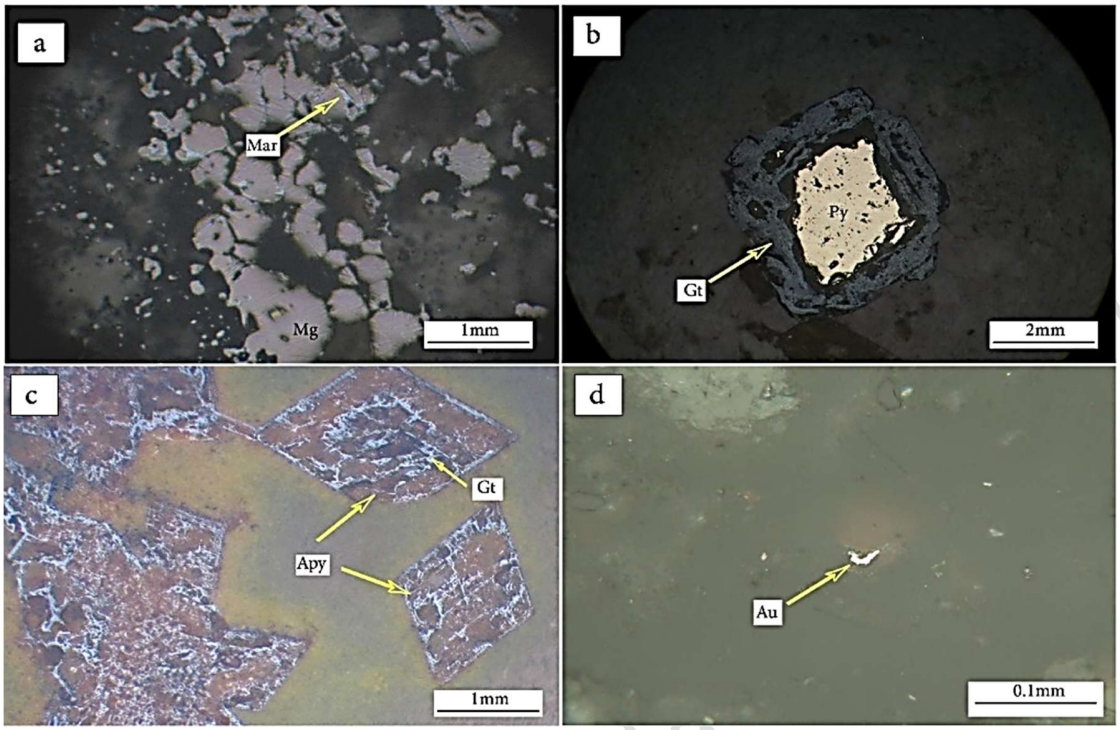

Fig. 4 Photomicrographs of samples showing (a) Magnetite replaced by martite (b) pyrite altered to goethite (c) arsenopyrite altered to goethite (d) gold, Gt: Goethite; Py: Pyrite; Mar: Martite; Mt: Magnetite; Au: Gold; Apy: Arsenopyrite.

According to the field and microscopic studies, there are both an alkaline rhyolitic dome and a subvolcanic granophyric mass, both of which can be the origin of silica solutions in mineralization. The presence of void-filling, streaky, scattered, alternate and selective textures in the host rock of the Hesar prospecting area indicates the epigenetic origin of mineralization. Sometimes, the association of quartz grains with ore materials, during replacement inside veins, seems that the related mineralization has been done selectively. In this way, mineralization can be seen inside the semi-volcanic mass of rhyodacite. Mineralization has been carried out in the second stage and selectively.

4.1.1. Alteration

Biotite alteration: This alteration type occurs in the vicinity of deep faults, and silicification and sericitization are significant. A large amount of pyrite has also been developed as veins and scattered in the rock (Fig. 5a).

Epidote alteration: From the center-east of the area and from the south to the north of Saridagh Mountain, Epidote alteration has occurred on both sides of the Aidoqmosh River. Epidote, along with chlorite, calcite, and quartz, are the constituent minerals of this alteration. The host rocks of the alteration are trachy-basalt volcanic rocks and porphyry to mega-porphyry basalt (Fig. 5b).

Argillic alteration: Indicating that argillic alteration is exposed/observed in small and scattered outcrops. In the center-west of the area, this alteration has been observed along with siliceous veins and siliceous zones. The host to this alteration is the tuff and agglomerate unit. The trend of these changes is N-S and NE-SW. Montmorillonite, kaolinite, quartz, and sericite are among the constituent minerals of this alteration. several faults are the cause of this alteration. (Fig. 5c, d).

Silicification in the area is formed through different trends. In some parts, these variations correspond to the argillic alteration. Quartz, kaolinite, sericite, and pyrite are the constituent minerals of this alteration. This type of alteration is mostly seen in the vicinity of faults and among volcanic rocks, tuff, and dacite. This phenomenon can be attributed to the final stages of volcanic processes in the region and the infiltration of hot siliceous solutions in the rocks surrounding the deposit. Gold mineralization is directly related to this alteration (Fig. 5e).

The alteration zones were investigated using Asteroid satellite images and were identified in the Hesar area. There is sericite, argillic, and goethite alteration types in the area that have a favorable outcrop. Based on field observations, thin sections, and X-ray diffractometry (XRD) studies, alteration zones include silicification, sulfidation, argillic, sericitization, and iron hydroxide. The argillic alteration is expanded in the study area, as shown in Fig. 3. Silicification, as an index alteration for epithermal gold deposition, is also observed in the area.

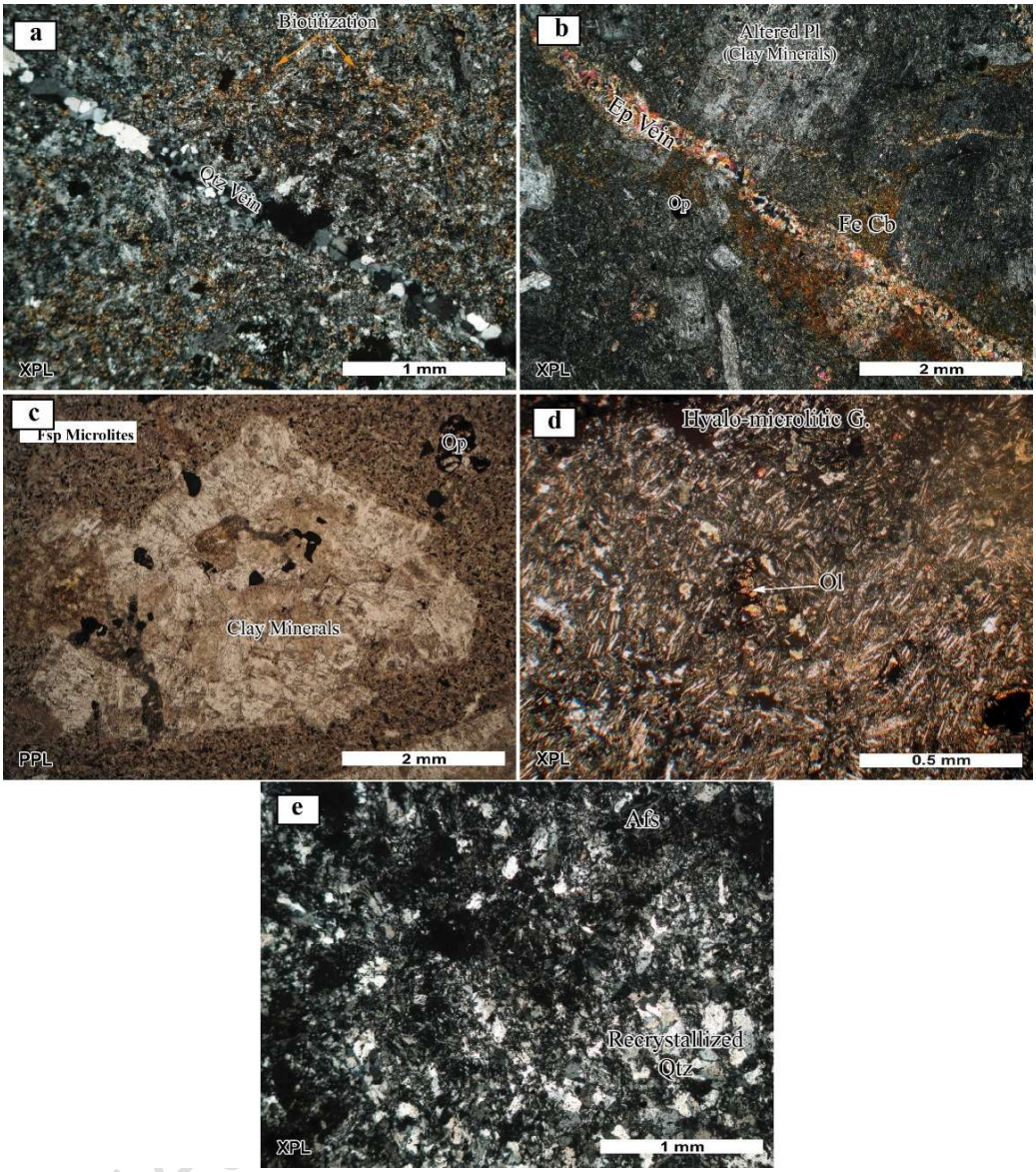

Fig. 5. (a) Biotite alteration, (b) Epidote alteration, (c, d) Argillic alteration, (e) Silicic alteration. Abbreviations: Qtz: Quartz; Ep: Epidote; Ol: Olivine; OP: Opac.

4.1.2. Mineral paragenesis in two phases, including:

A. First stage

In this phase, magnetite is seen as scattered grains or sometimes in a mass form. In some areas, magnetite has been transformed into minerals such as martite due to oxidation. In this mineral phase, pyrite is rarely seen (Fig. 4a).

B. Second stage

This phase is of sulfide type, and its symbol is pyrite mineral, and during decomposition, it has produced secondary products of iron hydroxide, including goethite, and it is scattered on the cross-section surface (Fig. 4b).

Arsenopyrite crystals are found in rhomboid form, completely replaced by iron hydroxides. Iron hydroxide products such as goethite, are formed from the decay of pyrite and arsenopyrite minerals and are not related to the decay of magnetite, and it is related to the second phase of mineralization (Fig. 4c).

In the first phase of mineralization, the dominant mineral is magnetite, which is interrupted by the second phase of sulfide mineralization of pyrite-type mineralization and related hydroxide products (goethite) in subsequent processes. The main mineralization in the Hesar mining area is related to the second phase and is of gold-bearing pyrite type. In most cases, pyrite mineral has produced iron hydroxide secondary products such as goethite during decomposition. In some cases, pyrite crystals have completely converted to iron hydroxide.

Free gold particles, dispersed and in a very small amount, which is the result of the decomposition of gold-bearing pyrite and arsenopyrite, can be seen in the silica veins (Fig. 4d). According to the location of the samples and the results of the analyses, gold mineralization has occurred at the intersection of faults in the margins of rhyolitic and rhyodacite volcanic rocks.

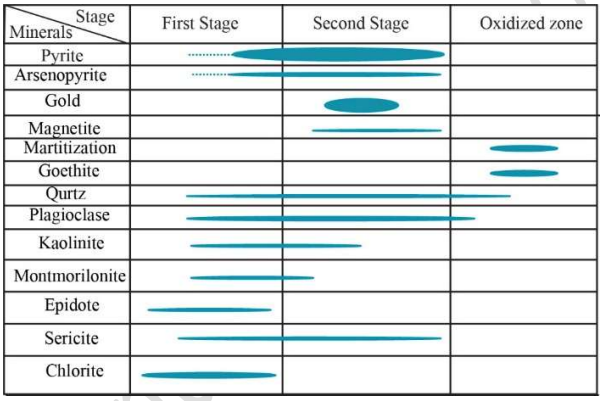

Fig. 6. Paragenetic sequence of minerals in the Hesar area

4.2. Fluid Inclusion

The petrographic study of fluid inclusions can help identify complex relationships between fluid inclusions and ore minerals (Roedder 1984; Goldstein and Reynolds 1994; Van den Kerkhof and Hein 2001). Fluid inclusions can be characterized by the appearance of their insert: properties such as size, shape, color, refractive index, and especially different phases at room temperature (Van den Kerkhof and Hein 2001). These fluids have different shapes, but to some extent, follow the mineral crystallization hexagonal system in quartz (Shepherd et al. 1985). In this study, fluid inclusions in the Hesar system have been studied in detail.

Fluid inclusions, in low abundance and with different distributions, are present in the study area. These data show that their size in the double-polished sections varies in the range of 5 to 30 microns, most of which are smaller than 20 microns. The shapes observed in the fluid inclusions are often irregular, elliptical, elongated, negative crystal, and wide.

4.2.1. Petrography

There are five types of fluid inclusions at room temperature based on the homogenization characteristics. The classification of primary fluid inclusions was performed according to Roedder (1984) and Van den Kherkof and Hein (2001), as demonstrated in (Fig. 7 a-e):
Type A: Liquid single-phase (L).
Type B: Gas single-phase (V).
Type C: Liquid-rich two-phase (L+V).
Type D: Gas-rich two-phase (V+L).
Type E: Liquid-rich three-phase with daughter minerals (V+L+S) as a rare type.
The abundance of type A is very low and can be detected in an irregular form in most cases. Based on this study, in this type, they are mostly amorphous and elongated. According to Samson and Walker (2000), probably the coexistence of type B with type C, D indicates boiling. Type C has the largest volume among fluid inclusion types which is between 10 and 35% of the fluids' volume. These three types are more frequent than the other types of fluid inclusions with larger sizes.
The gas bubbles are more than 70% of the fluid volume in type D. Homogeneity to the gas phase occurs at short intervals with a filling degree of less than 45%. Type D is less frequent than the type C fluid inclusions and They are mostly seen with irregular shapes. The last type is type E. There are daughter minerals that are surrounded by liquids, as shown in Fig. 7e. The E-type fluid inclusions are rare in comparison with the other types of fluid inclusions.

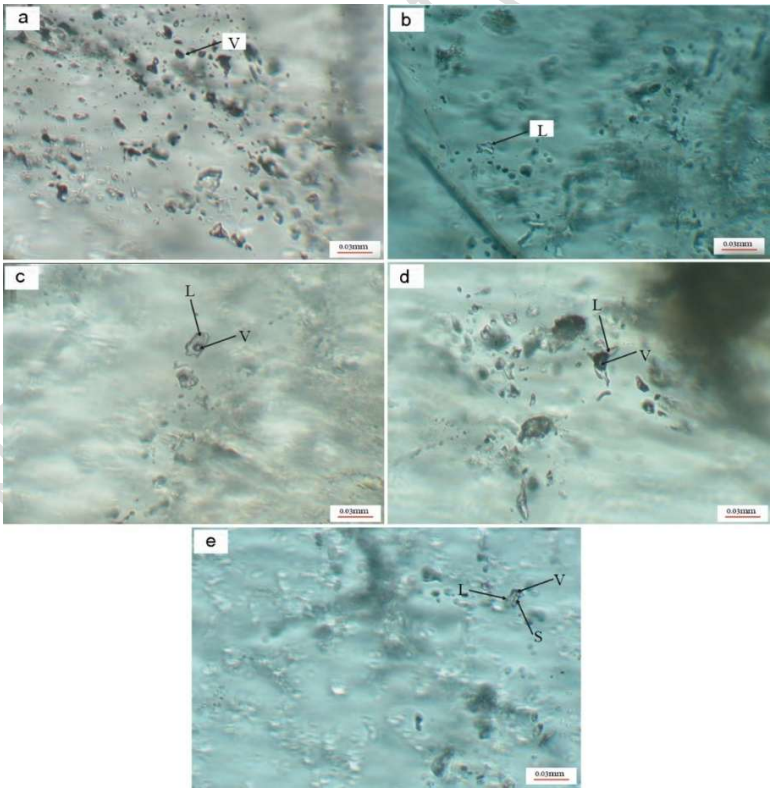

Fig. 7. Photomicrographs of fluid inclusions in quartz from Hesar deposit: (a) Vapor-only phase, (b) Liquid-only phase by liquid-rich two-phase fluid inclusion, (c) Liquid-rich two-phase fluid inclusion, (d) Vapor-rich two-phase fluid inclusion (boiling), (e) Solid-bearing fluid inclusion. Abbreviations: L :Liquid; V: Vapor; S: Solid.

4.2.2. Temperature, salinity and density

After completing the petrographic study of the fluid inclusions, the most important step is thermometry, which is performed to obtain the physicochemical conditions of ore-forming solutions during ore deposition. This method is the most important and widespread method of non-destructive analysis in fluid inclusions (Shepherd et al. 1985).

In this research, microthermometry was performed on 108 primary fluid inclusions, without cutting tails, in the quartz samples of the study area, using Linkam THMSG 600 device in the Microthermometry Laboratory of Tarbiat Modares University with the ability to measure in the temperature range of -196 to +600°C.

In liquid-rich and gas-rich two-phase fluid inclusions, microthermometric studies include; First is freezing and then heating. The final freezing of the inclusions was done in the temperature range of -100 to -105°C to ensure that all phases were frozen. Then increase the temperature insert: was increased until the first melting point of ice (Te or Tmf) is revealed. This temperature indicates the solutes in the sample. As the temperature continues to increase, the ice in the inclusion bar is melted until the last ice crystal melts, which is called the last melting point of ice (or Tm_{ice}), which indicates the amount of salinity (wt.% NaCl equiv.). Then, upon reaching room temperature, the heating process starts, and this temperature increase continues until the steam bubble in the sample becomes homogenized, at the homogenization temperature (Th), which indicates the minimum temperature of ore formation and mineralization.

The T_mf in the Hesar system shows a range of -21 to -61°C with the highest frequency in the range of -53 to -55°C, as illustrated in Fig. 8a. It is CO_2 with a small amount of CH_4 or N_2 based on T_mf values (Touret 1981), which represents fluid closure in the H_2O-NaCl-CO_2 ternary system (Borisenko et al. 1997) (Table 1).

In liquid-rich and gas-rich two-phase fluid inclusions Analyzed, the $T_m$ice are between -9 and -1.1°C with a high frequency in the range of -4 to -1.5°C (Fig. 8a). The T_h values varied between 140 and 260°C, with the highest frequency in the range of 160-200°C, as shown in Fig. 8b. Based on the T_m values, the salinity is calculated using the equation provided by Bodnar and Vityk (1994). It is between 0.18 and 14 wt.% NaCl equiv., which is most common in the range of 2 to 6% (Fig. 8c) (Table 1).

The fluid density can be calculated with a relative approximation (Zhang and Frantz 1987) by the salinity and the melting temperature. In this case, the density of the fluid can be obtained using the isolines in the salinity-melting temperature diagram which are from 0.8 to 1 g/cm^3 (Fig. 8d). Bivariate plots of homogenization temperature versus salinity (Fig. e8) further demonstrate that sulfide ligands were the dominant metal-transporting agent in the mineralizing fluids of the Hesar.

Table 1. Microthermometric data of fluid inclusions of quartz associated with mineralization horizons the Hesar area.

sample	Mineral	phase	type	Tice	salinity	TH	Teut
Stage 1	Qurtz	L+V V+L	p	-9 TO -5.8 -8 TO -10	8 TO 13 11.5 TO 13.8	210 TO 260 240 TO 250	-52- TO -61
Stage 2	Qurtz	L+V V+L	p	-0.1 TO -6 -5.3 TO -2	0.2 TO 8.5 4 TO 8	134 TO 234 180 TO 220	-55 TO -58

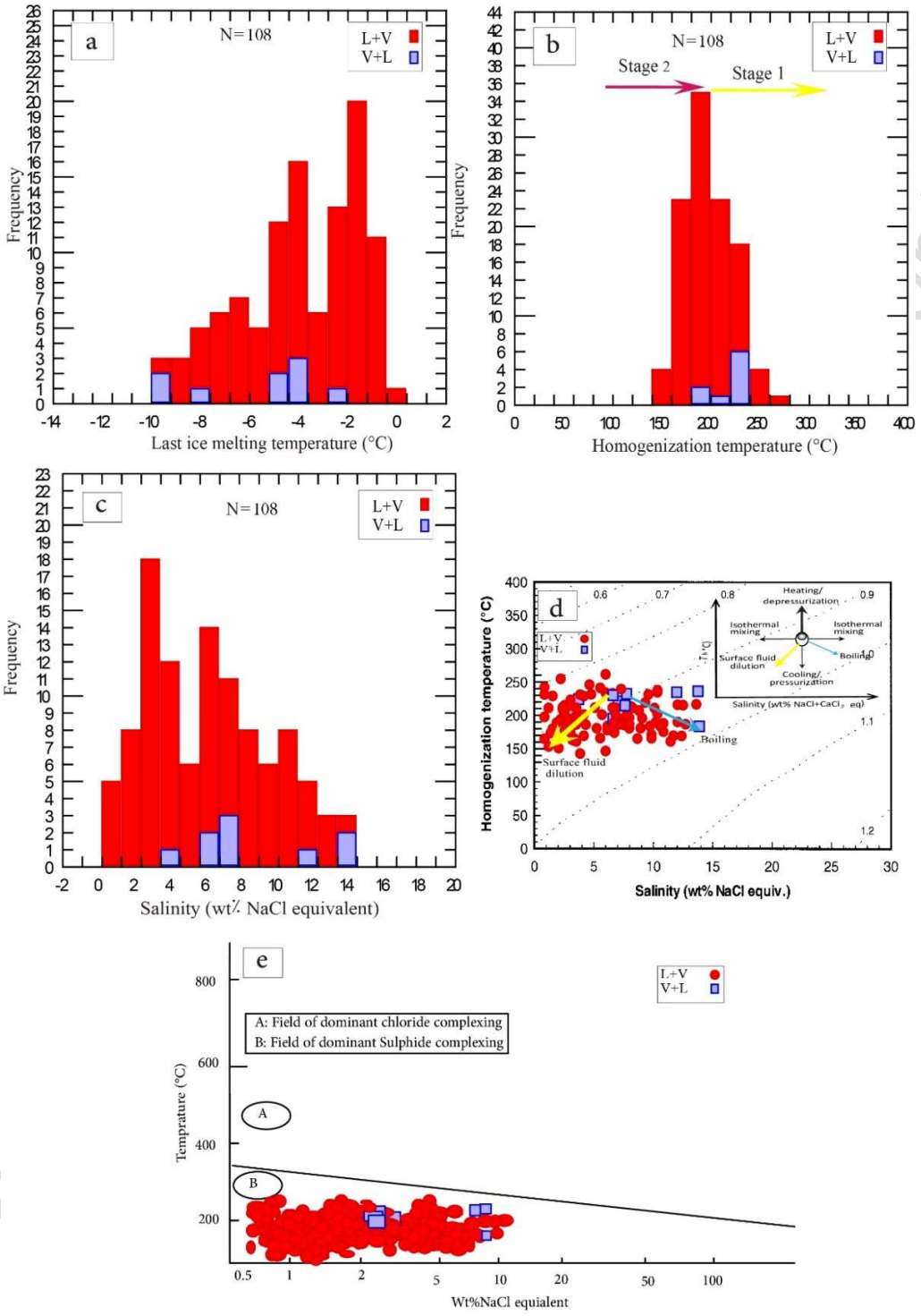

Fig. 8. (a) Histogram of last ice melting temperature (Tm), (b) Homogenization Temperature (Th), (c) Salinity in fluid inclusions measured in quartz, (ed) Fluid inclusion density diagram in quartz from Hesar iron deposit (Zhang and Frantz, 1987),

4.2.3. Raman spectroscopy

Six measurements were performed by Raman laser spectroscopy on the types C and D, as depicted in Fig 9. The spectra obtained indicate the presence of water as the main solution, especially in type C. This analysis confirmed the presence of H_2O in gas-rich fluid inclusions (Type D). Moreover, the existence of CO_2 and CH_4 in the fluid inclusions type C in the gas part was also confirmed. Based on a comparison between pure water and type C peaks, the type C as liquid-rich (L+V) fluid inclusion is not pure water and contains salt.

Controlled chemistry in the NaCl-H_2O system in the Fluid Inclusion Laboratory of Leoben, Austria, was chosen as the first test according to the study by Caumon et al. (2015). The salinity was calculated based on a relation between 0.2 wt.% NaCl equiv. and molality using the Labspec software for the Horiba Jobin Yvon instrument (Bodnar 2003).

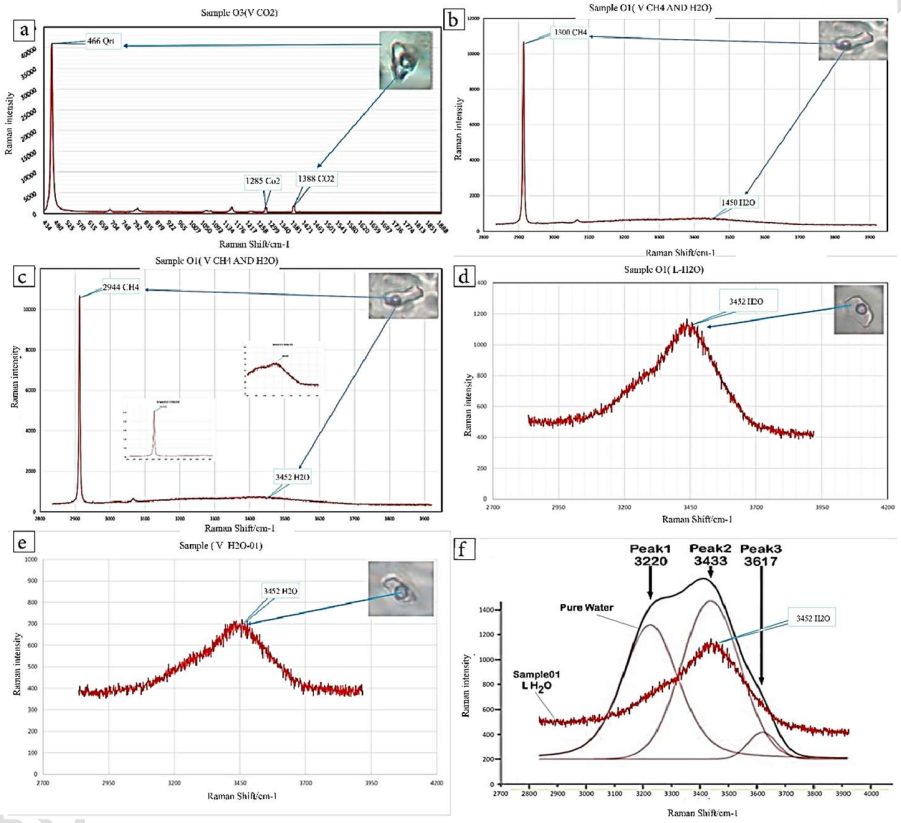

Fig. 9. a) Raman spectroscopy peaks for fluid inclusions rich in CO2 gas, in the quartz mineral, b,c) Raman spectroscopy peaks for fluid inclusions rich in CH4 gas in H2O context, d,e) Raman spectroscopy peaks for fluid inclusions by liquid water along with water gas vapor, f) Comparison between pure water peaks and results of Raman analysis of the fluid inclusion sample for type C .

Caumon et al. (2015) plotted a salt molality calibration curve relative to the two peak intensities (I_{3425}/I_{3260}) resulting from Raman spectroscopy analysis on a large number of samples with various concentrations of NaCl. The ratios are then implemented on the diagram, leading to the molality/mol.kg^{-1} values (Fig. 9 f).

The salinity is calculated using molality (Bodnar 2003) through several microthermometric analyses on fluid inclusions with various ratios of water and NaCl solution (the salinity is equal to the 'A' constant (4.514) multiplied by the molality). Using this, and the values from Fig. 10, the salinities from the Hesar area vary between 1.69 and 8.8 wt.% NaCl, as shown in Table 2. These salinities are similar to those obtained by the microthermometric study.

Based on the calculation of salinity using molality by Bodnar (2003), the following equation was introduced:

Salinity = A × Molality (1)

Where A is a constant of 4.514, salinities varied between 1.69 and 8.8 mass% NaCl equiv., as shown in Table 2. These salinities are similar to salinities obtained by the microthermometric study, which represent epithermal mineralization according to Wilkinson's (2001)

Table 2. Calculated salinities based on molality for samples from the Hesar area.

Sample	Fluid inclusion type	mol.kg^{-1} (molality)	Salinity = A × Molality (wt.% NaCl equiv.)
A	Type C	1.95	1.95*4.514=8.8
B	Type C	1.06	1.06*4.514=4.78
C	Type C	0.375	0.375*4.514=1.69

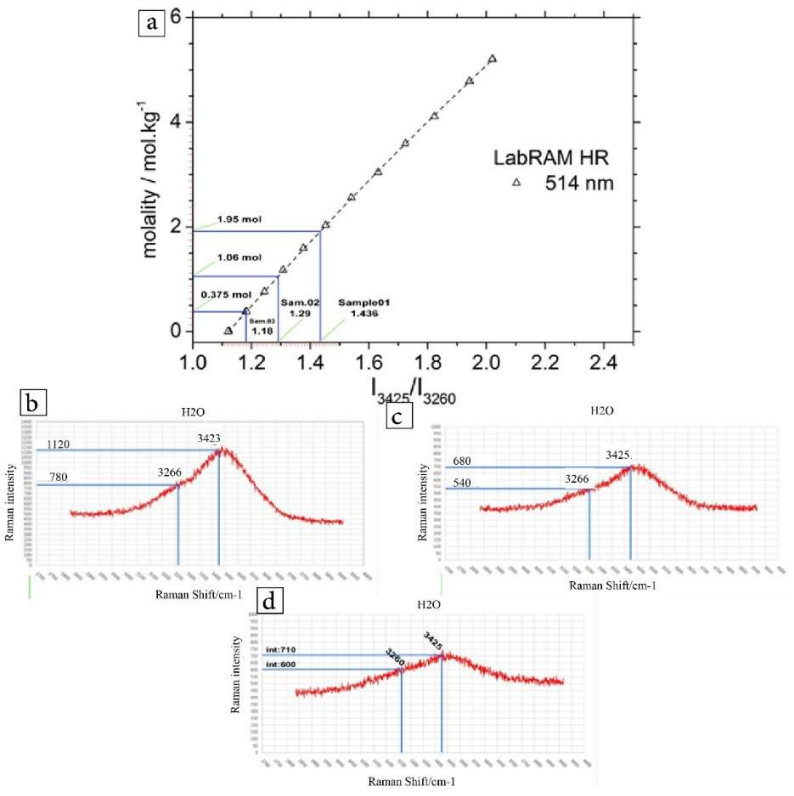

Fig. 10. a) Molality (mol.kg_1) of NaCl solutions as a function of Raman intensity ratio (I_{3425}/I_{3260}), laser radiation, and spectrometer. Uncertainties are smaller than or equal to the data point size. Dashed lines are second-order polynomial fit functions (Caumon et al. 2013). The ratio of I_{3425}/I_{3260} for the three samples of H_2O was plotted. Raman spectroscopy peaks for type C fluid inclusions which include I_{3260} and I_{3425} values for samples number 1 (b), 2 (c), and 3 (d).

4.3. Sulfur isotopes

The sulfur stable isotope study is of particular importance to determine the origin and conditions of the formation of sulfide deposits, and with its help, the influence of magmatic or non-magmatic activities on the genesis of the deposits can be investigated (Hoefs 2021). It is the origin that changes as a result of the passage of time and variations in the physicochemical conditions (temperature, pH, and oxygen fugacity) of the environment.

six pyrite and four Chalcopyrite samples from quartz veins were sulfur isotope analyzed at the Arak University. After combustion of the bulk sample in the elemental analyzer, the generated SO_2 gas passes through the system and column and is stripped of the water in the water trap as well as SO_2 in the purge and trap column. The adsorption column is then heated to 220℃ to release any accumulated SO_2 gas. This gas ultimately enters the IRMS. In EA-IRMS, the mass ratio of 66/64 is determined to evaluate the $^{34}S/^{32}S$ ratio of the sample.

The lowest $\delta^{34}S$ value for pyrite samples is -7.6‰, and the highest value is -2.8‰; the lowest $\delta^{34}S$ value for chalcopyrite samples is -3.8‰, and the highest value is 2.4‰ (Table 3).

Table 3. Sulfur isotope ($\delta^{34}S$) data from the Hesar area

Sample no.	Mineral	δ34S CDT (‰)	T (˚C)	1000 ln α	δ34S H2S fluid (‰)
MH1	Pyrite	-1	200	1.8	-2.8
MH2	Pyrite	-1.1	200	1.8	-2.9
MH3	Pyrite	-2.4	200	1.8	-4.2
MH4	Pyrite	-5.8	200	1.8	-7.6
MH5	Pyrite	-4.7	200	1.8	-6.5
MH6	Pyrite	-5.3	200	1.8	-7.1
MH7	Chalcopyrite	-2	200	1.8	-3.8
MH8	Chalcopyrite	1	200	1.8	0.8
MH9	Chalcopyrite	-1.3	200	1.8	-3.1
MH10	Chalcopyrite	4.2	200	1.8	2.4

4.4. Oxygen isotopes

The value of $\delta^{18}O$ in nature varies up to 100‰, and half of this range is found in meteoric waters. Chondrites have a very limited range of $\delta^{18}O$ values, the value of $\delta^{18}O$ in the mantle is 5.7 ±0.3‰, and it seems that it has been constant over time for the Earth and the Moon (Taylor, 1980). The range of $\delta^{18}O$ of meteoric waters is between +5.7 to -40‰. In the case of $\delta^{18}O$, the range of magma water is between +5.7 and 10‰. In general, the continental crust is enriched with ^{18}O compared to the Earth's mantle, which is mostly the result of the long-term interaction of the continental crust and the oceanic crust and the distribution of ^{18}O inside the crust minerals during low-temperature geological processes (Rollinson 2005).

Since temperature controls the isotopic separation of stable isotopes between the mineral and hydrothermal fluids, and as previously demonstrated, the average formation temperature of quartz derived from the fluid inclusion study method was determined to be 200°C, it is therefore possible to calculate the approximate $\delta^{18}O$ of the fluid in equilibrium with quartz (Clayton and Keiffer, 1991).

For $\delta^{18}O$ analysis, eight mineralized quartz samples – previously characterized for temperature and salinity – were equilibrated with CO_2 gas. The resulting CO_2 was introduced via dual-inlet isotope ratio mass spectrometry (IRMS), where $^{18}O/^{16}O$ ratios were determined by measuring m/z 46/44 ion beam intensity. The values obtained from the oxygen-stable isotope analysis in the quartz from the Hesar area are given in Table 4. By placing the temperature obtained from the thermometry of fluid inclusions, the values of $\delta^{18}O_{H2O}$ for quartz samples have been calculated. $\delta^{18}O$ values of the quartz samples vary between -1.8 and -3.7‰ (Table 4).

Table 4. Oxygen ($\delta^{18}O$) isotope data from the Hesar area.

Sample name		Mineral	$\delta^{18}O$ (‰) V-SMOW	T (˚C)	$\delta^{18}O$ H_2O (‰)
ske062c		Quartz	6.5	200	-2.3
ske063c		Quartz	5.9	200	-2.9
ske064c		Quartz	7.1	200	-1.7
ske065c		Quartz	5.1	200	-3.7
ske066c		Quartz	6.5	200	-2.3
ske067c		Quartz	5.4	200	-3.4
ske068c		Quartz	7.3	200	-1.5
ske069c		Quartz	6.2	200	-2.6

5. Discussion

5.1. Ore-forming fluids and soulfur sorces

The difference in fluid density is of special importance because the fluid flow process is affected by its density (Wilkinson 2001). Therefore, using the salinity diagram of the fluid inclusions against the homogenization temperature. The density variations show the two processes of cooling and boiling in the transformation process of ore-forming hydrothermal fluid. The process of cooling, decreasing the uniform temperature, causes an increase in the density and decrease in the velocity of the mineral fluid, and finally causes the deposition and concentration of minerals, while the fluid inclusions formed from boiling as a result of the temperature decrease or pressure decrease lead to the formation of a denser fluid with salinity.

Fluid inclusion studies on quartz from the Hesar gold deposit indicate salinities of 1–14 wt% NaCl equiv. Homogenization temperatures of the ore-forming fluids range from 134°C to 260°C. Estimated pressures are <10 bars, corresponding to a fluid trapping depth of ~500 m below the paleosurface. Fluid densities range from 0.8 to 1.0 g/cm³. which is typical for epithermal deposits (Fig. 8f).

Inclusions of trapped boiling fluids commonly show the characteristics of high-density brine, low-density vapor, and intermediate-density solution that occur in the same regions of the same samples (e.g., Ramboz et al. 1982; Simmons and Browne 2000; Ouyang et al. 2014). This explanation has been used to account for other epithermal systems such as those in Japan, New Zealand, and Mexico (e.g., Scott and Watanabe 1998; Simpson et al. 2001; Camprubí and Albinson 2007; Kouhestani et al. 2015).

377

Gold, which forms complexes with sulfur (Seward 1973), precipitates at shallower depths where boiling causes H_2S loss (Brown 1986; Hedenquist and Henley 1985). H_2S is much more soluble than CO_2 and, when it exsolves, CO_2 had already been completely lost and pH suffers no major changes (Henley et al. 1984). So, it is a drop-in sulfur fugacity and temperature which triggers gold precipitation (Brown 1986; Simmons and Browne 2000). Similarly, the CO_2 loss triggers a rapid crystallization of calcite, favoring the formation of the tabular habit (e.g., André-Mayer et al. 2002).

The narrow range of $\delta^{34}S$ isotopic ratio changes can indicate the sulfur isotopic equilibrium state in the deposits of this area. The co-growth of sulfide minerals in the stages of mineralization and the closeness of their $\delta^{34}S$ values indicate that these minerals were probably formed under equilibrium conditions and isotopic separation was the cause of the difference in their sulfur isotopic values (Fig. 11). Putting the analytical results in the reference chart and comparing it with other types of mineralization shows that the gold mineralization at Hesar is of epithermal type. Sulfur is sourced from magmatic activity, as evidenced in Figure 11.

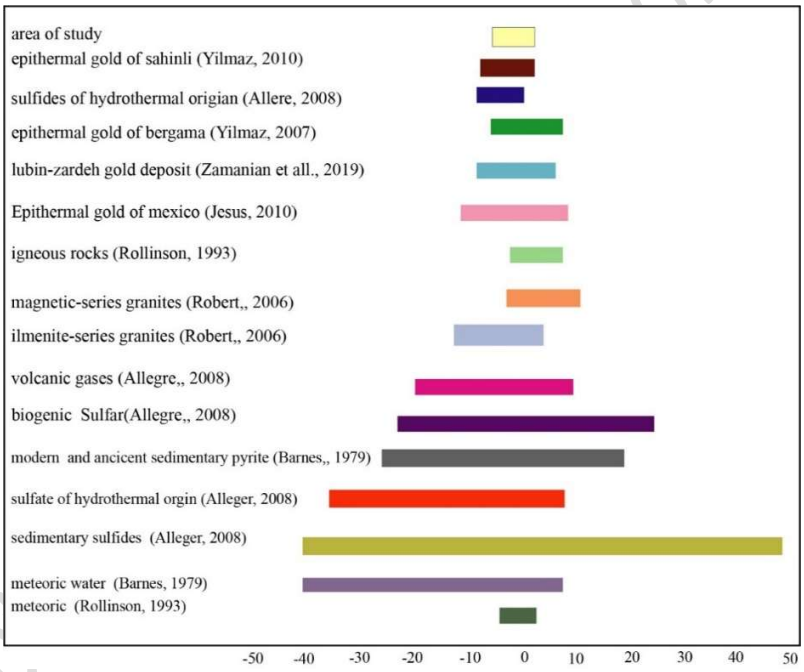

Fig. 11. Sulfur isotope ($\delta^{34}S$) data from the Hesar area compared to those from several epithermal deposits and various sources (Hoefs, 2004)

Determining the origin of ore solution, using oxygen isotope in the Hesar prospecting area the origin of the ore solution in different alteration zones has been investigated by different researchers on various deposits based on the evidence of fluid inclusions and stable isotopes. It is possible to calculate $\delta^{18}O$ values of the fluid that has reached isotopic equilibrium with quartz. As seen in Table 3, the fluid in equilibrium with quartz in these temperature ranges has $\delta^{18}O$ values between -1.8 and -3.7‰, so the $\delta^{18}O$ values of this fluid are mainly in the range of meteoric water.

This $\delta^{18}O$ isotopic value is similar to many other global epithermal ore deposits, such as the low-sulfidation type in Bergama, Turkey (Yilmaz et al. 2019), North Xinjiang, northwest China (Chen et al. 2014), and in South China Block (Zhong et al. 2016; Fig. 12-13).
In this study, the calculated $\delta^{18}O$ values for water equilibrated with quartz range is from -1.8 to -3.7‰.
As has been shown for the earlier parts of this paper, the dominant mechanism for gold precipitation at Hesar was the mixing of deep ascending fluids with cooler inflow meteoric waters in permeable zones at a depth of less than 500 m. Mixing occurred between a hot, saline (avg. 9.84 wt.% NaCl) and deeply circulating ^{18}O-enriched magmatic water (avg. 4.45‰) of stage I and a cool, low-salinity and shallow inflow meteoric water which is relatively ^{18}O-depleted (−7‰; e.g., Faure et al. 2005).

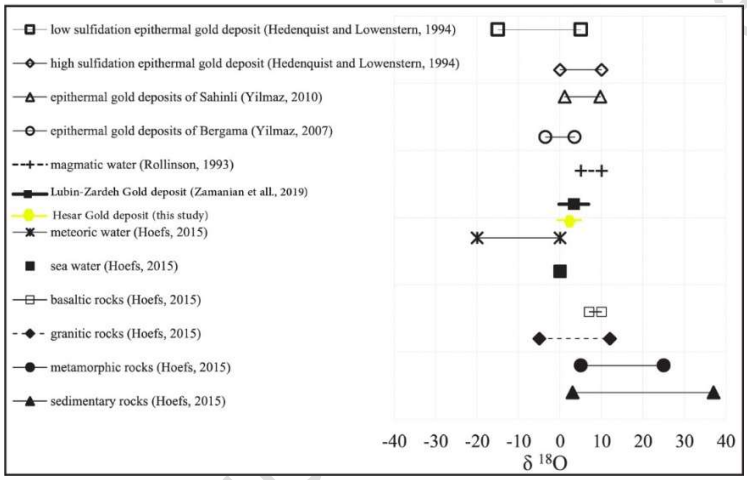

Fig. 12. $\delta^{18}O$ isotopic data from Hesar gold deposits relative to important references. All isotopic values in permil (SMOW), Distribution of $\delta^{18}O$ values obtained for different sulfide minerals hosted in quartz of the Hesar gold deposit.

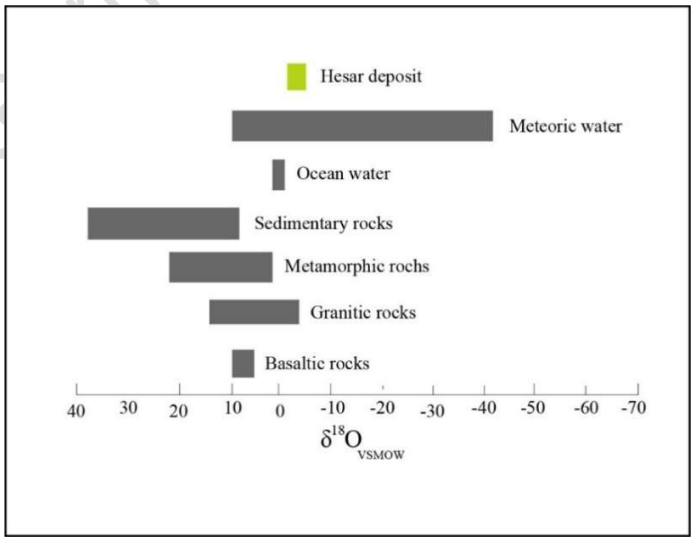

Fig. 13. $\delta^{18}O$ values of the Hesar deposit compared to important geological reserves (Hoefs, 2021)

5.2. Trapping pressure and mineralization depth

The diagram demonstrates that this mineralization process occurred at a depth of about 430 meters at the Hesar deposit in Fig. 14a. The formation depth for the epithermal deposits is estimated based on the presence of liquid-rich and vapor-rich two-phase fluids using boiling point with depth curve as shown in Fig. 14b (Hass, 1971).

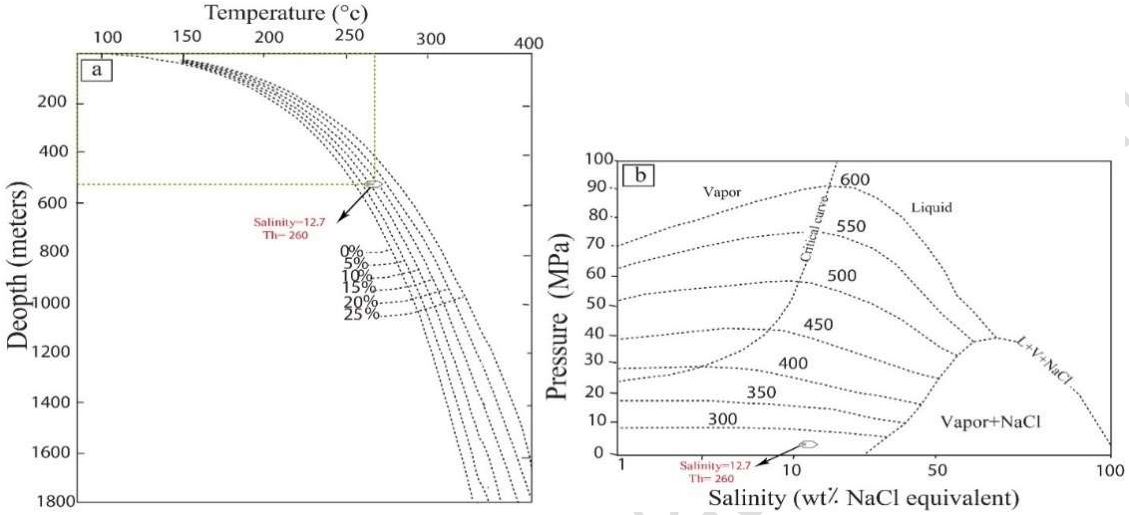

Fig. 14. (a) The diagram of depth versus homogenization temperature with salinity isograds to determine the depth of the boiling event in the Hesar gold deposit (after Hass, 1971. (b)

5.3. Evolution of ore-forming fluids

The cooling trend observed in the Hesar deposit probably reflects the regressive evolution of the mineralization system in a high-temperature phase. It is followed by gradual cooling and cold surface water flow inside the system, resulting in dilution and reducing the temperature rising process (Fig. 15).

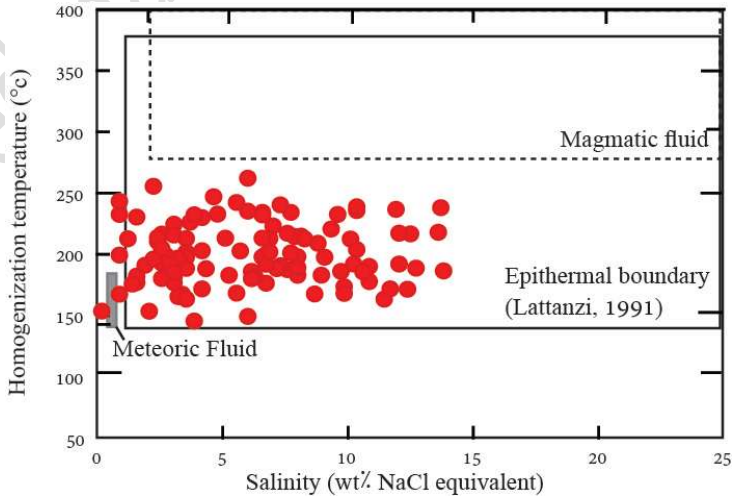

Fig. 15. Diagram of salinity dispersion and homogeneity temperature of fluid inclusions in Hesar gold quartz (Lattanzi 1991; Hedenquist and Arribas 1998; Naden et al. 2005)

6. Conclusions

The lithology of the host rocks at the Hesar gold deposit comprises volcanic and intrusive igneous rocks. Mineralization occurs epigenetically as fracture-filling along faults and fractures, and as vein-veinlet systems within the igneous rocks. Core logging, mineral associations, and textural studies indicate two distinct stages of mineralization.

Fluid inclusion studies on quartz from the Hesar gold deposit show salinities ranging from 1 to 14 wt% NaCl equiv., with the most frequent values between 2–6 wt% NaCl equiv. Homogenization temperatures of ore-forming fluids range from 134°C to 260°C, with the dominant interval being 160–200°C. Estimated pressures are <10 bars, corresponding to a trapping depth of approximately 500 meters below the paleosurface.

The ore-forming fluids originated from magmatic solutions mixed with meteoric water. Sulfur isotope analyses of sulfide minerals indicate a sulfur source derived from the region's igneous rocks. Oxygen isotope values from deposit quartz further support a magmatic fluid origin with meteoric mixing.

Integrated petrographic studies, paragenetic sequence analysis, fluid inclusion data, and stable isotope (O, S) results collectively demonstrate that the Hesar deposit likely formed from hydrothermal solutions. The ore fluids were primarily magmatic in origin with significant meteoric water input. This mixing process resulted in mineralization consistent with an epithermal deposit type.

Acknowledgments:
The authors would like to thank Kambiz Mohajeran from Kavosh Kani Mohajer Consultant Engineers for sharing data and providing invaluable guidance. Sina Asadi from Shiraz University is thanked for the Raman data and Mahya Manouchehry is appreciated for processing the fluid inclusion data.

References

Aghazadeh M, Hou Z, Badrzadeh Z, Zhou L (2015) Temporal-spatial distribution and tectonic setting of porphyry copper deposits in Iran: Constraints from zircon U–Pb and molybdenite Re-Os geochronology. *Ore Geology Reviews 70: 385-406.* https://doi.org/10.1016/j.oregeorev.2015.03.003

Aghanabati, A., 2004. The Geology of Iran. National Geology and Exploration Organization, 586 pp. Retrieved Retrieved September 25, 2024 from https://www.researchgate.net/publication/292808705_Geology_of_Iran_Tehran_Iran

Alirezaei S, Ebrahimi S (2011). Geological setting, alteration, and fluid inclusion characteristics of Zaglic and Safikhanloo epithermal gold prospects, NW Iran, *Geological Society* London Special Publications 350(1):133-147.

Aliyari F, Afzal P, Lotfi M, Shokri S, Feizi H (2020) Delineation of geochemical haloes using the developed zonality index model by multivariate and fractal analysis in the Cu-Mo porphyry deposits. *Applied Geochemistry 121: 104694.* https://doi.org/10.1016/j.apgeochem.2020.104694

Asadi HH, Voncken JHL, Kühnel RA, Hale M (2000) Petrography, mineralogy and geochemistry of the Zarshuran Carlin-like gold deposit, northwest Iran, *Mineralium Deposita*, 35, 656–671.

Ashrafi N, Jahangiri A, Hasebe N, Eby GN (2018) Petrology, geochemistry and geodynamic setting of Eocene-Oligocene alkaline intrusions from the Alborz-Azerbaijan magmatic belt, NW Iran. *Geochemistry 78: 432-461.* https://doi.org/10.1016/j.chemer.2018.10.004

Ashrafpour E, Ansdell K, Alirezaei S (2012) Hydrothermal fluid evolution and ore genesis in the Arghash epithermal gold prospect, northeastern Iran, *Journal of Asian Earth Sciences*, 51(2) 60-44. https://doi.org/10.1016/j.jseaes.2012.01.020

Asiabanha A, Foden J (2012) Post-collisional transition from an extensional volcano-sedimentary basin to a continental arc in the Alborz Ranges, N-Iran. *Lithos 148: 98-111.* https://doi.org/10.1016/j.lithos.2012.05.014

Bark G, Boyce AJ, Fallick AE, Weihed P (2020) Fluid and metal sources in the Fäboliden hypozonal orogenic gold deposit, Sweden. *Mineralium Deposita 56: 425-440.* 10.1007/s00126-020-00977-7

Barnes HL (1997) Geochemistry of hydrothermal ore deposits. 3rd ed, New York, *John Wiley & Sons, 972.*

Berberian M, King GCP (1981) Towards a paleogeography and tectonic evolution of Iran. *Canadian Journal of Earth Sciences 18: 1764-1766.* https://doi.org/10.1139/e81-019.

Bodnar RJ (2003) Introduction to aqueous fluid systems. In: Samson I, and Anderson A, Marshall D. (Eds.), Fluid Inclusions, Analysis and Interpretation, *Mineral, Assoc, Canada, Short Course 32: 81–99.*

Bodnar RJ, Vityk MO (1994) Fluid inclusions as tectono-thermobarometers: Relation between pressure-temperature history and re-equilibration morphology during crustal thickening. Geology 22 (8): 731–734. https://doi.org/10.1130/0091-7613(1994)022<0731:FIATRB>2.3.CO;2

Borisenko AS, Kholmogorov AI, Borovikov AA, Shebanin AP, Babich VV (1997) Composition and metallization of ore-forming fluids at the Deputatskoe tin-ore deposit (Yakutia). *Geologiya i Geofizika (Russian Geology and Geophysics) 38 (11): 1860-1871.*

Brown, JD. (1986). Evaluations of self and others: Self-enhancement biases in social judgments. *Social Cognition, 4*(4), 353–376. https://doi.org/10.1521/soco.1986.4.4.353

Camprubí, A., and Albinson, T (2007) Epithermal deposits in México—Update of current knowledge, and an empirical reclassification, in Alaniz-Álvarez, S.A., and Nieto-Samaniego, Á.F., eds., Geology of México: Celebrating the Centenary of the Geological Society of México: *Geological Society of America Special* 422, p. 377–415, doi: 10.1130/2007.2422(14).

Caumon MC, Tarantola A, Mosser-Ruck R (2015) Raman spectra of water in fluid inclusions: I. Effect of host mineral birefringence on salinity measurement. *Journal of Raman Spectroscopy 46(10): 969–976.* https://doi.org/10.1002/jrs.4708

Chen YJ, Santosh M (2014) Triassic tectonics and mineral systems in the Qinling Orogen, central China, *Special Issue,* 49, 338-358

Clayton RN, Mayeda TK, Goswami J.N, Olsen E J (1991) Oxygen isotope studies of ordinary chondrites *Geochimica et Cosmochimica Acta* 55, 8, 2317-2337

Cooke AR, Simmons SF (2000) Characteristics and genesis of epithermal gold deposits, *Economic Geology* 13-https://doi.org/10.5382/Rev.13

Faure M, Mézème EB, Duguet M, Cartier C (2005) Paleozoic tectonic evolution of medio-Europa from the example of the French Massif Central and Massif Armoricain, *Journal of the virtual Explorer*,10.3809/jvirtex.2005.00120.

Ghasemi Siani M, Lentz DR, Nazarian M (2020) Geochemistry of igneous rocks associated with mineral deposits in the Tarom-Hashtjin metallogenic province, NW Iran: An analysis of the controls on epithermal and related porphyry-style mineralization. *Ore Geology Reviews* 126: 103753. https://doi.org/10.1016/j.oregeorev.2020.103753

Giles D, Marshall B (2004) Genetic significance of fluid inclusions in the CSA Cu-Pb-Zn deposit, Cobar, Australia. *Ore Geology Reviews 24 (3-4): 241-266.* https://doi.org/10.1016/j.oregeorev.2003.05.003

Goldstein RH, Reynolds TJ (1994) Systematics of fluid inclusions in diagenetic minerals. *Society for Sedimentary Geology, Short Course 31: 188*.

Haschke M, Ahmadian J, Murata M, McDonald I (2010) Copper mineralization prevented by arc-root delamination during Alpine-Himalayan collision in central Iran. *Economic Geology 105 (4): 855–865*. https://doi.org/10.2113/gsecongeo.105.4.855

Hass JL (1971) The effect of salinity on the maximum thermal gradient of a hydrothermal system at hydrostatic pressure. *Economic Geology 66: 940–946.* https://doi.org/10.2113/gsecongeo.66.6.940

Hassanpour Sh, Moazzen M (2017) Geochronological constraints on the Haftcheshmeh porphyry Cu-Mo-Au ore deposit, central Qaradagh batholith, Arasbaran metallogenic belt, northwest Iran. *Acta Geologica Sinica 91: 2109–2125*. https://doi.org/10.1111/1755-6724.13452

Hedenquist J, Arribas A (1998) Evolution of an intrusion-centered hydrothermal system; Far Southeast-Lepanto porphyry and epithermal Cu-Au deposits, Philippines, *Economic Geology 93: 373-404*. https://doi.org/10.2113/gsecongeo.93.4.373

Hedenquist J, Henley A (1985) Exploration for Epithermal Gold Deposits *SEG Reviews* 13, 245-277

Hedenquist J, Lowenstern JB (1994) The role of magmas in the formation of hydrothermal ore deposits. *Nature 370: 519–527*. https://doi.org/10.1038/370519a0

Hedenquist JW, Arribas AR, Gonzalez-Urien E (2000) Exploration for Epithermal Gold Deposits. *Society of Economic Geologists 13*.

Henley R,WTruesdell AH, Barton PB (1984) FLUID-MINERAL EQUILIBRIA IN HYDROTHERMAL SYSTEMS *Society of Economic Geologists* 1

Hitzman MW (2000) Source basins for sediment-hosted stratiform Cu deposits: implications for the structure of the Zambian Copper belt. *Journal of African Earth Sciences 30 (4): 855–863*. https://doi.org/10.1016/S0899-5362(00)00056-7

Hoefs, J., 2004. Stable isotope geochemistry. Spinger-Verlag, Berlin, 244. https://doi.org/10.1007/978-3-540-70708-0

Hoefs J (2021) Stable Isotope Geochemistry. *Springer-Verlag, Berlin, 9th edition*.

Jebeli, M, Afzal P, Pourkermani M, Jafari Rad A (2020) Characteristics of fluid inclusions in the Cenozoic volcanic-hosted Kushk-e-Bahram Manto-type Cu deposit of central Iran. *Geologos 26: 127–137*.

Jiang L, Xue C, Li W, Xiang K, Wang B (2020) Geological and geochemical constraints on the genesis of the Bengge gold deposit in the Yidun Terrane, SE Tibet. *Journal of Asian Earth Sciences 195: 104338*. https://doi.org/10.1016/j.jseaes.2020.104338

Kavosh Kani Mohajer Consultant Engineers (2004) Exploration of epithermal and placer gold in Hesar, north of the city of Mianeh,: 275.

Kouhestani H, Ghaderi M, Chang Z, Zaw K (2015) Constraints on the ore fluids in the Chah Zard breccia-hosted epithermal Au–Ag deposit, Iran: Fluid inclusions and stable isotope studies *Ore Geology Reviews*, 65 (2), 512-521. https://doi.org/10.1016/j.oregeorev.2013.06.003

Kouhestani H, Ghaderi M, Chang Z, Zaw K (2015) Constraints on the ore fluids in the Chah Zard breccia-hosted epithermal Au–Ag deposit, Iran: Fluid inclusions and stable isotope studies, *Ore Geology Reviews,* 65 (2) 512-521. https://doi.org/10.1016/j.oregeorev.2013.06.003

Kouhestani H, Mokhtari MAA, Qin K, Zhang X (2020) Genesis of the Abbasabad epithermal base metal deposit, NW Iran: Evidences from ore geology, fluid inclusion and O–S isotopes. *Ore Geology Reviews 126: 103752*. https://doi.org/10.1016/j.oregeorev.2020.103752

Lattanzi P (1991) Applications of fluid inclusions in the study and exploration of mineral deposits. *European Journal of Mineralogy 3(4): 689-702*. https://doi.org/10.1016/0375-6742(91)90068-6.

Liu Y, Yang L, Wang S, Liu X, Wang H, Li D, Wei P, Cheng W, Chen B (2019) Origin and evolution of ore-forming fluid and gold-deposition processes at the Sanshandao gold deposit, Jiaodong Peninsula, eastern China. *Minerals 9: 189-214*. https://doi.org/10.3390/min9030189

Long DA (2002) The Raman Effect: A Unified Treatment of the Theory of Raman Scattering by Molecules. *John Wiley & Sons, Ltd,: 640*.

McMillan PF (1989) Raman spectroscopy in mineralogy and geochemistry. *Annual Review of Earth and Planetary Sciences 17: 255-279*. https://doi.org/10.1146/annurev.ea.17.050189.001351

Mehrabi B, Ghasemi Siani M, Goldfarb R, Azizi H, Ganerod M, Erin Elizabeth Marsh b (2016) Mineral assemblages, fluid evolution, and genesis of polymetallic epithermal veins, Glojeh district, NW Iran, *Ore Geology Review*s,78, 41-57.

Mishra B, Pruseth KL, Hazarik P, Chinnasamy SS (2018) Nature and source of the ore-forming fluids associated with orogenic gold deposits in the Dharwar Craton. *Geoscience Frontiers 9: 715-726*. https://doi.org/10.1016/j.gsf.2017.09.005

Mousavi Motlagh SH, Ghaderi M (2019) The Chargar Au-Cu deposit: an example of low-sulfidation epithermal mineralization from the Tarom subzone, NW Iran. *Neues Jahrbuch für Mineralogie (Journal of Mineralogy and Geochemistry) 196(1): 43-66*. https://doi.org/10.1127/njma/2019/0158

Mousavi Motlagh SH, Ghaderi M, Yasami N (2021) Porphyry-type mineralization associated with epithermal deposits in the Tarom metallogenic belt of NW Iran: Constraints from fluid

inclusions. *Journal of Geochemical Exploration 223: 106724.* https://doi.org/10.1016/j.gexplo.2021.106724

Nabatian G, Ghaderi M, Neubauer F, Honarmand M, Liud X, Dong Y, Jiang Sh, Quadt A, Bernroider M (2014) Petrogenesis of Tarom high-potassic granitoids in the Alborz-Azarbaijan belt, Iran: Geochemical, U-Pb zircon and Sr-Nd-Pb isotopic constraints. *Lithos 184-187: 324-345*. https://doi.org/10.1016/j.lithos.2013.11.002

Naden J, Kilias SP, Darbyshire DPF (2005) Active geothermal systems with entrained seawater as modern analogs for transitional volcanic-hosted massive sulfide and continental magmato-hydrothermal mineralization: The example of Milos Island, Greece. *Geology 33(7): 541-544*. https://doi.org/10.1130/G21307.1

Ouyang H, Mao J, Zhou Z, Huiming S (2015) Late Mesozoic metallogeny and intracontinental magmatism, southern Great Xing'an Range, northeastern Chin, *Gondwana Research*, 27, 1153-1172, https://doi.org/10.1016/j.gr.2014.08.010

Pokrovski G, Akinfiev NN, Borisova AY, Zotov A, Kouzmanov K (2014) Gold speciation and transport in geological fluids: Insights from experiments and physical-chemical modelling. *Geological Society, London, Special Publication 402: 9-70.*

Rabiee A, Rossetti F, Tecce F, Asahara Y, Azizi H, Glodny J, Lucci F, Nozaem R, Opitz J, Selby D (2019) Multiphase magma intrusion, ore-enhancement and hydrothermal carbonatisation in the Siah-Kamar porphyry Mo deposit, Urumieh-Dokhtar magmatic zone, *NW Iran. Ore Geology Reviews 110: 102930*. https://doi.org/10.1016/j.oregeorev.2019.05.016

Ramboz C, Pichavant M, Weisbrod A (1982) Fluid immiscibility in natural processes: Use and misuse of fluid inclusion data: II. Interpretation of fluid inclusion data in terms of immiscibility, *Chemical Geology*, 37, 29-48. https://doi.org/10.1016/0009-2541(82)90065-1

Richards JP (2015) Tectonic, magmatic and metallogenic evolution of the Tethyan orogen: From subduction to collision, *Ore Geology Reviews 70: 323-345.* https://doi.org/10.1016/j.oregeorev.2014.11.009

Richards JP (2015) The oxidation state, and sulfur and Cu contents of arc magmas: implications for metallogeny. *Lithos 233: 27-45*. https://doi.org/10.1016/j.lithos.2014.12.011

Richards JP, Sholeh A (2016) The Tethyan Tectonic History and Cu-Au Metallogeny of Iran. *Society of Economic Geologists, Special Publication 19: 193-212.*

Roedder E (1984) Fluid inclusions. Reviews in mineralogy, *Mineralogical Society of America,: 644*. https://doi.org/10.1515/9781501508271-001.

Rollinson P (2005). Using Peer Feedback in the ESL Writing Class, *ELT Journal*, 59, 23-30. https://doi.org/10.1093/elt/cci003

Rye RO, Bethke PM, Wasserman MD (1992) The stable isotope geochemistry of acid sulfate alteration, *Economic Geology*, 87 (2): 225–262. https://doi.org/10.2113/gsecongeo.87.22-25.

Samson IM, Walker RT (2000) Cryogenic Raman spectroscopic studies in the system NaCl-$CaCl_2$-H_2O and implications for low-temperature phase behavior in aqueous fluid inclusions. *Canadian Mineralogist 38 (1): 35-43*. https://doi.org/10.2113/gscanmin.38.1.35

Scott AM, Watanabe Y (1998) Extreme boiling model for variable salinity of the Hokko low-sulfidation epithermal Au prospect, southwestern Hokkaido, Japan. *Mineralium Deposita*, 33, 568-578.

Seward TM (1973) Thio complexes of gold and the transport of gold in hydrothermal ore solutions Geochimica, *et Cosmochimica Acta*, 37 (3) 379-399. https://doi.org/10.1016/0016-7037(73)90207

Shafiei B, Haschke M, Shahabpour J (2009) Recycling of orogenic arc crust triggers porphyry Cu mineralization in Kerman Cenozoic arc rocks, southeastern Iran. *Mineralium Deposita 44(3): 265–283*. https://doi.org/10.1007/s00126-008-0216-0

Shahbazi S, Ghaderi M, Afzal P (2021) Prognosis of gold mineralization phases by multifractal modeling in the Zehabad epithermal deposit, NW Iran. *Iranian Journal of Earth Sciences 13(1): 31-40*. https://doi.org/10.30495/ijes.2021.678957

Shahbazi S, Ghaderi M, Alfonso P (2019) Mineralogy, alteration and sulfur isotope geochemistry of the Zehabad intermediate-sulfidation epithermal deposit, NW Iran. *Turkish Journal of Earth Sciences 28(6): 882-901*. https://doi.org/10.3906/yer-1902-1

Shamanian GH, Hedenquist JW, Hattori KH, Hassanzadeh J (2004) The Gandy and Abolhassani epithermal prospects in the Alborz magmatic arc, Semnan province, Northern Iran *Economic Geology*, 2: 275-294.

Shepherd TJ, Rankin AH, Alderton DHM (1985) A practical guide to fluid inclusion studies. *Blackie, London,: 239.* https://doi:10.1180/minmag.1986.050.356.32.

Sholeh A, Rastad E, David Huston D, Bruce Gemmell J, Ryan D (2016) The Chahnaly Low-Sulfidation Epithermal Gold Deposit, Western Makran Volcanic Arc, Southeast Iran, *Economic Geology*, 111 (3): 619–639. https://doi.org/10.2113/econgeo.111.3.619

Simmons DTA, Symons TB, Sangster DF (2000) Paleomagnetism of the Socieyu Cliffs dolostone and the age of the Nanisivk zinc deposits, Baffin Island, Canada. *Mineralum Deposita 35: 672-682*. https://doi:10.1007/s001260050270

Simmons SF, Browne PRL (2000) Hydrothermal minerals and precious metals in the Broadlands–Ohaaki geothermal system: implications for understanding low-sulfidation epithermal environments, *Economic Geology* 95 (5): 971–999.

Simon C, Ripley M (2011) The Role of Magmatic Sulfur in the Formation of Ore Deposits. *Reviews in Mineralogy and Geochemistry 73(1): 513-578*.

Simpson MP, Simmons SF, Mauk J, (2001) The mineral products of boiling in the golden cross epithermal deposit. *New Zealand Minerals and Mining Conference Proceedings*, 209-216.

Stampfli M (2000) Tethyan oceans. *Geological Society of London 173: 1-23*.

Stöcklin J (1974) Possible ancient continental margins in Iran. *The Geology of Continental Margins, Springer,: 873-887*.

Stöcklin J, Eftekhar-Nezhad J (1969) Geological map of Zanjan, scale 1:250,000, No. D4-61. *Geological Survey of Iran, Tehran, Iran.*

Taylor HPJR (1980) *The effects of assimilation of country rocks by magmas on $^{18}O/^{16}O$ and $^{87}Sr/^{86}Sr$ systematics in igneous rocks. Earth and Planetary Science Letters 47(2): 243-254*. https://doi.org/10.1016/0012-821X (80) 90040-0.

Touret J (1981) Fluid inclusions in high-grade metamorphic rocks. In: Hollister LS, and Crawford ML. (Eds.), A Short Course in Fluid Inclusion: Applications to Petrology, *Mineralogical Association of Canada 6: 182-208*.

Van den Kerkhof AM (1988) The System CO–CH–N in 242 Fluid Inclusions: Theoretical Modelling and Geological Applications. Ph.D. Thesis, *Vrije Universiteit Amsterdam, The Netherlands,: 206*.

Van den Kerkhof AM, Hein UF (2001) Fluid inclusion petrography. *Lithos 55: 27-47.* https://doi:10.1016/S0024-4937(00)00037-2.

Walrafen GE (1962) Raman spectral studies of the effects of electrolytes on water. *Journal of Chemical Physics 36: 1035-1042*. https://doi.org/10.1063/1.1732628

Wilkinson JJ (2001) Fluid inclusions in hydrothermal ore deposit. *Lithos 55: 229-72.* https://doi.org/10.1016/S0024-4937(00)00047-5

Yasami N, Ghaderi M (2019) Distribution of alteration, mineralization and fluid inclusion features in porphyry-high sulfidation epithermal systems: The Chodarchay example, NW Iran. *Ore Geology Reviews 104: 227-245*. https://doi.org/10.1016/j.oregeorev.2018.11.006

Yasami N, Ghaderi M, Madanipour S, Taghilou B (2017) Structural control on overprinting high-sulfidation epithermal on porphyry mineralization in the Chodarchay deposit, northwestern Iran. *Ore Geology Reviews 86: 212-224.* https://doi.org/10.1016/j.oregeorev.2017.01.028

Yılmaz F, Özdemir N, Demirak A, Tuna AL (2019) Heavy metal levels in two fish species Leuciscus cephalus and Lepomis gibbosus Southeast Anatolian Orogenic Belt revisited Canadian**,** *Journal of Earth Sciences*, 56 (11): 1163–1180.

Zarasvandi A, Liaghat S, Zentilli M (2005) Geology of the Darreh-Zerreshk and Ali-Abad porphyry copper deposits, Central Iran. *International Geology Review 6: 620-646.* https://doi.org/10.2747/0020-6814.47.6.620

Zhang YG, Frantz JD (1987) Determination of the homogenization temperatures and densities of supercritical fluids in the system NaCl-KCl-$CaCl_2$-H_2O using synthetic fluid inclusion. *Chemical Geology 64: 335-350*. https://doi.org/10.1016/0009-2541(87)90012-X

Zhao JH, Zhang SHB, Wang XL, Research P (2008) Neoproterozoic geology and reconstruction of South China, *Precambrian Research,* 309, 1-5 https://doi.org/10.1016/j.precamres.2018.02.004

Zhong J, Wang S, Gu DZ, Cai YQ, Fan HH, Shi ChH, Hu ChN (2016) Geology and fluid geochemistry of the Na-metasomatism U deposits in the Longshoushan uranium metallogenic belt, NW China: Constraints on the ore-forming process *Ore Geology Reviews* 116, 103-214